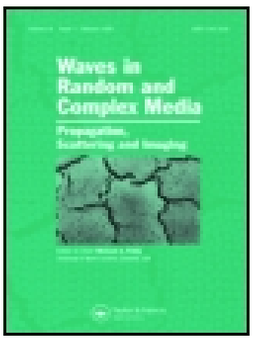

Waves in Random and Complex Media

ISSN: (Print) (Online) Journal homepage: https://www.tandfonline.com/loi/twrm20

A device of XOR logic gate and multiscale sensing based on layered topology

Jun-Yang Sui, You-Ming Liu & Hai-Feng Zhang

To cite this article: Jun-Yang Sui, You-Ming Liu & Hai-Feng Zhang (2023): A device of XOR logic gate and multiscale sensing based on layered topology, Waves in Random and Complex Media, DOI: 10.1080/17455030.2023.2169389

To link to this article: https://doi.org/10.1080/17455030.2023.2169389

Published online: 24 Jan 2023.

WAVES IN RANDOM AND COMPLEX MEDIA
https://doi.org/10.1080/17455030.2023.2169389

Taylor & Francis
Taylor & Francis Group

A device of XOR logic gate and multiscale sensing based on layered topology

Jun-Yang Sui[a], You-Ming Liu[b] and Hai-Feng Zhang[a]

[a]College of Electronic and Optical Engineering & College of Flexible Electronics (Future Technology), Nanjing University of Posts and Telecommunications, Nanjing, People's Republic of China; [b]Bell Honors School, Nanjing University of Posts and Telecommunications, Nanjing, People's Republic of China

ABSTRACT

In this paper, a multiscale non-reciprocity device based on the layered topology of one-dimensional (1-D) photonic crystals is studied, which can meet the functions of XOR logic gate, magnetic field sensing and refractive index sensing. Modulating by the external magnetic fields, sharp transmission peak (TP) is obtained in the terahertz (THz) range (the value of TP is more than 0.9), by changing the two different magnetic fields applied to the particular medium layers, TP enables XOR logic phenomena at the same frequency point. Simulation shows that with the detection of physical quantities changes, the frequency point of TP will vary. Therefore, through the location of TP, the sensing functions of magnetic field and refractive index can be realized, moreover the optimum performances of quality factor (QF), sensitivity (S), the figure of merit (FOM), and the detection limit (DL) belonging to them are 1323.45, 0.01 $(2\pi c/d_0)$/T, 35.93 T^{-1}, 1.39×10^{-3} T and 1381.88, -0.0061 $(2\pi c/d_0)$/RIU, 13.57 RIU^{-1}, 3.7×10^{-3} RIU. Additionally, the device also realizes the non-reciprocity of electromagnetic waves (EWs) via the introduction of magneto-optical media InSb and the change of EWs incident angle, which means that XOR logic gate, magnetic field, and refractive index sensing detection respectively have positive and negative scales.

ARTICLE HISTORY
Received 5 August 2022
Accepted 9 January 2023

KEYWORDS
Optical sensors; logic gate; non-reciprocity; magnetic field detection; refractive index detection

1. Introduction

Photonic crystals (PC) are a new type of electromagnetic medium that can be divided into one-dimensional (1-D), two-dimensional, and three-dimensional arrangements [1], and have been the subject of continuity in in-depth theoretical and experimental research [2–4]. PC have the photonic band gaps (PBGs) [5–7], which, like the electronic band gaps in semiconductors, can prohibit the propagation of electromagnetic waves (EWs), but a large number of studies have proved that when the defect layer is introduced, it can destroy the symmetry of the photonic crystals layered topology (PCLT), changing the band structure of the PCLT, and generating new electromagnetic patterns within the PGB, so that EWs can propagate in PCLT at specific frequency bands [8,9]. Moreover, compared with the periodic structure, the quasi-periodic PCLT has more adjustable parameters in the structural design

CONTACT Hai-Feng Zhang hanlor@163.com

[10,11], which is more conducive to the use of PBG to obtain transmission peaks (TP) and has the advantages of simple structure, compact size, strong flexibility, convenient design, and manufacturing. As a result, it has gained more attention in many areas such as sensors [12], logic gates [13,14], and so on.

As a high electron mobility semiconductor material with a gyratory frequency in the terahertz (THz) range, InSb increases the non-reciprocity of EWs in positive and negative propagation due to its dispersion and gyratory properties and the magneto-optical effect exhibited under the action of magnetic fields [15,16], which makes InSb widely studied and used in THz isolators and absorbers. Based on the cyclotron characteristics of InSb in the THz band, Fan et al. proposed a tunable THz isolator with a periodic structure of semiconductor magnetic plasma, which had the advantages of non-mutual easiness, low loss, and high isolation bandwidth [17]. Wan et al. studied unidirectional absorbers with narrow band angle polarization-sensitive regions based on the quasi-periodic structure of InSb, using PBG to generate a wide band of absorption bands and whose polarization separation and non-reciprocal ability could be adjusted by temperature and magnetic induction intensity [18]. In addition, the enhancement of non-reciprocal phenomena is closely related to the increase in the angle of the incident light, the increase in the frequency of plasma rotation, the decrease in the thickness of the magneto-optical medium, and the opposite direction of the external magnetic field [19].

As research continues to advance, PC devices that can be used for logic gate and physical quantity detection are widely studied. Fatima et al. designed an all-optical AND logic gate using the combination of universal NAND gates. The structure was composed of a hexagonal arrangement of air holes in silicon and had a response period of 6.48 ps and a bit rate of 0.154 TB/sec to perform logical operations [20]. Sharma et al. proposed an ultrafast full-beam XOR and XNOR logic gate based on a photonic crystals fiber (PCF) nonlinear optical loop mirror, and the highly nonlinear PCF with flat dispersion could obtain a numerical analysis speed of 1 TB/s [21]. Yan et al. came up with a refractive index (RI) sensing model of PCF based on the surface plasma resonance effect, which could monitor the RI of liquid materials by wrapping a later of gold nanofilm on the elliptical air pore on the left side of the PCF core as a sensing peer for surface plasma resonance, and the RI monitoring range is 1.43–1.49, the sensitivity (*S*) is as high as 12719.97 nm/RIU, and the *S* was good [22]. The above work is of great significance to the development of the field of PC for the logic calculation and physical quantity detection. Unfortunately, these studies only have a single function, and there is currently very little research on PC devices that combine logic gate and physical quantity detection, which also limits the research ideas in related fields.

The design of this work is a 1-D PCLT that integrates the logic gate and physical quantity detection functions and has two scales: positive and negative. Magnetized InSb is introduced as a defect layer to destroy the symmetry of PCLT and produce a sharp TP with a high-quality factor (QF). By applied magnetic fields regulation, the presence or absence of the TP (the value of TP is more than 0.9) can be determined, thus realizing the XOR logic gate function. With the change of the applied magnetic field and the RI of the medium layers, the normalized angular frequency point (NAFP) corresponding to the TP will move with it and has a good linear fitting relationship (LFR) which owns high *S*, high the figure of merit (FOM), and low detection limit (DL), through the position of TP, the detection of weak alters in the magnetic field or the RI can be realized. And one of the highlights of this paper is that the designed device has a non-reciprocal function, through the magneto-optical effect of

InSb and the increase of the incidence angle of EWs, the non-reciprocal phenomenon of TP obtained in opposite directions is obvious, which means that the magnetic field and RI detection of the back and forth scale can be realized under the condition of ensuring the XOR logic operation.

2. Structure design and simulation

The 1-D PCLT which can be fabricated by the etching method is shown in Figure 1 [23], which is composed of ordinary A, B, C, D, E, and F dielectrics for non-symmetrical arrangement, where A and B are periodic arrangements, and the numbers of the period are $N_1 = 7$, $N_2 = 5$, $N_3 = 5$, $N_4 = 5$, 'EFE' is a filter structure. Moreover, the magneto-optical medium InSb layers are introduced into the original structure as defects, and its entire structure is exposed to 270 K of air to adapt to the general situation. To represent them clearly, different dielectrics are filled here with different colors. EWs are incidents from the positive and negative directions, respectively, represented by red and blue arrows, forming an angle with the *xoz* plane and the angle of incidence is expressed by θ, where $\theta = 30°$, to achieve the purpose of enhancing non-reciprocity, which will be explained later. This paper uses the normalized thickness d_0, the value of which is 10 μm. Also, the angular frequency ω is normalized, and the unit of ω is $(2\pi c/d_0)$, expressed by α. The thicknesses of the ordinary dielectrics A, B, C, D, E, and F are severally replaced by d_A, d_B, d_C, d_D, d_E, and d_F, and the parameter values of each other are $0.6d_0$, $0.4d_0$, $0.75d_0$, $0.7d_0$, $4.4d_0$, $4.6d_0$. The values of RI belonging to ordinary dielectrics are $n_A = 2.74$, $n_B = 1.4$, $n_C = 1.38$, $n_D = 1.5$, $n_E = 6.06$, and $n_F = 1$. The defect layers are composed of two different semiconductors $InSb_1$ and $InSb_2$, the thicknesses of which are $d_1 = 0.09d_0$ and $d_2 = 0.062d_0$, separately, due to the action of the external magnetic field, the dielectric of InSb behaves as an anisotropic tensor, so its RI varies with the strength of the magnetic field. Because the device has positive and negative scales, B_1 and B_2 are the external magnetic field applied vertically on $InSb_1$ and $InSb_2$ along the – y-axis on the positive scale and *y*-axis on the negative scale, respectively. For EWs positive propagation, $B_1 = 0.85$ T, $B_2 = 1.343$ T, and $B_1 = 0.695$ T, $B_2 = 1.3$ T

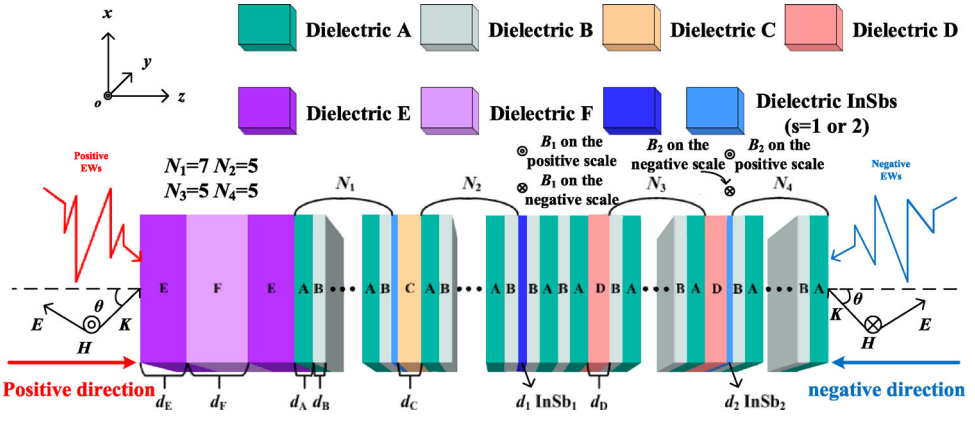

Figure 1. Schematic of the proposed PCLT which is made up of different dielectric layers. Two beams of EWs are incident from the positive and negative directions. The directions of the applied magnetic fields are marked with coordinate axis as the reference.

while EWs propagate negatively. It should be noted that our work mainly focuses on the theoretical model. Ordinary dielectrics are not affected by the external magnetic field, and the thicknesses of InSb layers are very thin compared with that of ordinary dielectric layers. Therefore, the magnetic field area exerted on the specific InSb layer is small, while other InSb layers are not affected. Considering the experimental application, Xuan et al. [24] designed a gradient magnetic field coil. By applying current to it, a spatial linear magnetic field can be generated, meeting the requirements of this paper that the magnetic field strength on diverse InSb layers is different and the effects of adjacent magnetic fields can be isolated. When EWs propagate in the 1-D PCLT, affected by Lorentz force, the external magnetic field mainly has a control function on TM polarized EWs [17], while the TE polarization is not controlled by the magnetic field. Therefore, this work will only focus on studying the PCLT performance under TM polarization and analyze the entire structure by the transfer matrix method [25,26].

InSb is an anisotropic material, and with the introduction of an external magnetic field, the effective dielectric constant of InSb is expressed as [3]:

$$\varepsilon_{TM} = \frac{\varepsilon_x^2 - \varepsilon_{xz}^2}{\varepsilon_x^2}, \tag{1}$$

where ϵ_x, ϵ_{xz} can be determined by the matrix of its dielectric function under TM polarization [27]:

$$\boldsymbol{\varepsilon}_{\mathbf{Insb}} = \begin{pmatrix} \varepsilon_x & 0 & \varepsilon_{xz} \\ 0 & \varepsilon_y & 0 \\ -\varepsilon_{xz} & 0 & \varepsilon_x \end{pmatrix}, \tag{2}$$

where [27]

$$\varepsilon_x = \varepsilon_\infty - \varepsilon_\infty \frac{\omega_p^2(\omega + i\nu_c)}{\omega[(\omega + i\nu_c)^2 - \omega_c^2]}, \tag{3}$$

$$\varepsilon_y = \varepsilon_\infty - \varepsilon_\infty \frac{\omega_p^2}{\omega(\omega + i\nu_c)}, \tag{4}$$

$$\varepsilon_{xz} = \varepsilon_\infty \frac{i\omega_p^2\omega_c}{\omega[(\omega + i\nu_c)^2 - \omega_c^2]}. \tag{5}$$

Among them, $\epsilon_\infty = 15.68$ is the high-frequency limit dielectric constant [28], $\omega_p = Ne^2/\epsilon_0 m^*$ is the plasma frequency, ϵ_0 and e respectively represent the dielectric constant and electron charge in the vacuum. m^* is the effective mass of the carrier, which is related to the mass of the electron m_e. For InSb, $m^* = 0.015m_e$. N is the intrinsic carrier density, which plays a critical role in the dielectric properties of InSb, as expressed in Equation (6). ν_c is the collision frequency of the carrier, which is separately expressed in ν_{c1} and ν_{c2} for $InSb_1$ and $InSb_2$, as well as $\nu_{c1} = 6 \times 10^{-5}\omega_p$ and $\nu_{c2} = 8 \times 10^{-6}\omega_p$ [27]. $\omega_c = eB/m^*$ is the electron gyration frequency, which is proportional to the intensity of the applied electric field [27].

$$N(m^{-3}) = 5.76 \times 10^{20} T_0{}^{1.5} \exp[-0.26/(2 \times 8.625 \times 10^{-5} \times T_0)], \tag{6}$$

as can be seen, by the equation, the temperature T_0 has a great influence on it. In addition, the RI of InSb is $n_{TM} = (\epsilon_{TM})^{1/2}$. Under TM polarization, the transfer matrix of InSb is

expressed as [3]:

$$\mathbf{M}_{TM} = \begin{pmatrix} \cos(k_{iz}d_i) + \dfrac{k_{ix}\varepsilon_{xz}}{k_{iz}\varepsilon_x}\sin(k_{iz}d_i) & -\dfrac{i}{\eta_i}\left[1 + \left(\dfrac{k_{ix}\varepsilon_{xz}}{k_{iz}\varepsilon_x}\right)^2\right]\sin(k_{iz}d_i) \\ -i\eta_i \sin(k_{iz}d_i) & \cos(k_{iz}d_i) - \dfrac{k_{ix}\varepsilon_{xz}}{k_{iz}\varepsilon_x}\sin(k_{iz}d_i) \end{pmatrix}, \tag{7}$$

where $k_{ix} = \omega/cn_{\mathrm{TM}}\sin\theta_i$ is the component of the wave vector on the x-axis, $k_{iz} = \omega/cn_{\mathrm{TM}}\cos\theta_i$ is the component of the wave vector in the z-axis, representing the wave vectors of $InSb_1$ or $InSb_2$, singly.and $\eta_i = (\epsilon_0/\mu_0)^{1/2}n_{\mathrm{TM}}/\cos\theta_i$ is the light conductivity, i is denoted by 1 or 2. Since ordinary dielectrics are not affected by applied magnetic fields, their transfer matrix is indicated as [29]:

$$\mathbf{M}_j = \begin{pmatrix} \cos(k_{jz}d_j) & -\dfrac{i}{\eta_j}\sin(k_{jz}d_j) \\ -i\eta_j \sin(k_{jz}d_j) & \cos(k_{jz}d_j) \end{pmatrix}, \tag{8}$$

where $k_{jz} = \omega/cn_j\sin\theta_j$ is the component of the wave vector on the z-axis, j can be indicated by A, B, C, D, E, and F, signified by different dielectric layer materials. Since PCLT is non-reciprocity, EWs propagate on positive and negative scales, corresponding to different transmission matrices, reflecting non-reciprocity. This article makes M_P the positive propagation transport matrix and M_N is homologous to the negative transport matrix, and their complete transport matrix expressions are as follows, where M_j (as shown in Equation (7)) represents the transfer matrices of dielectrics A, B, C, D, E, F, M_{TMi} (as show in Equation (8)) indicates the materials of $InSb_1$ and $InSb_2$.

The entire positive transfer matrix M_P is given as:

$$M_P = [M_E M_F M_E (M_A M_B)^{\mathbf{7}} M_{TM\mathbf{2}} \mathbf{M}_C (\mathbf{M}_A \mathbf{M}_B)^{\mathbf{5}} \mathbf{M}_{TM\mathbf{1}} (M_B M_A)^{\mathbf{2}} M_D (M_B M_A)^{\mathbf{5}} M_D M_{TM\mathbf{2}} (M_B M_A)^{\mathbf{5}}], \tag{9}$$

and the entire transfer matrix of the negative propagation M_N is gained as:

$$M_N = [(M_A M_B)^{\mathbf{5}} M_{TM\mathbf{2}} \mathbf{M}_D (\mathbf{M}_A \mathbf{M}_B)^{\mathbf{5}} \mathbf{M}_D (\mathbf{M}_A \mathbf{M}_B)^{\mathbf{2}} \mathbf{M}_{TM\mathbf{1}} (\mathbf{M}_B M_A)^{\mathbf{5}} \mathbf{M}_C \mathbf{M}_{TM\mathbf{2}} (\mathbf{M}_B \mathbf{M}_A)^{\mathbf{7}} \mathbf{M}_E \mathbf{M}_F \mathbf{M}_E]. \tag{10}$$

To obtain the transmittance, the transmittance coefficient of the PCLT should be obtained first, which is calculated as:

$$t = \frac{2\eta_0}{(m_{11} + m_{12}\eta_{N+1})\eta_0 + (m_{11} + m_{12}\eta_{N+1})}, \tag{11}$$

due to both sides of the PCLT are air, there is $\eta_0 = \eta_{N+1} = (\epsilon_0/\mu_0)^{1/2}n_0/\cos\theta_0$, the formula for calculating can be written as [3]:

$$T = |t|^2. \tag{12}$$

3. Analysis and discussion

The transmission spectra of the positive and negative scales XOR logic gate are shown in Figure 2, with the two external magnetic fields B_1 and B_2 respectively applied to $InSb_1$ and $InSb_2$. When a magnetic field is present, it is denoted by a logic level (LL) '1', otherwise LL is

'0' when a sharp TP exists, it is denoted by a LL of '1', and vice versa as '0'. For a more intuitive embodiment, 'In_1' indicates the state of existence of B_1, 'In_2' symbolizes the magnetic field B_2, and 'Ou_1' stands for the state of presence of TP. As can be seen from Figure 2(a), under the condition that EWs propagate in the positive direction when the applied magnetic field B_1 is present and B_2 is absent, transmissivity (T) is obtained and much greater than 0.9, the value of it is 0.9658, the NAFP corresponding to TP is 0.26496 α, and QF = 1379.98, forming a sharp TP. The states are '$In_1 = 1$', '$In_2 = 0$', and '$Ou_1 = 1$', related to the '1 XOR 0 = 1' of the XOR logic gate. When B_1 does not exist and B_2 exists, $T = 0.9301$, much greater than 0.9, QF = 659.21. The states are '$In_1 = 0$', '$In_2 = 1$', and '$Ou_1 = 1$' cohering with the '0 XOR 1 = 1' of the XOR logic gate. The TP of this case owns NAFP 0.26946 α, coinciding with '1 XOR 0 = 1', which is convenient for detecting logical operations. When both B_1 and B_2 are subsistent, TP does not exist, then '$In_1 = 1$', '$In_2 = 1$', and '$Ou_1 = 0$', and T is much less than 0.1, correlating to the XOR logical operation '1 XOR 1 = 1'. When neither B_1 nor B_2 is not existent, TP is absent and T is much less than 0.1, then '$In_1 = 0$', '$In_2 = 0$', and '$Ou_1 = 0$' corresponding to the '0 XOR 0 = 0' of the XOR logic gate. For EWs propagating in the opposite

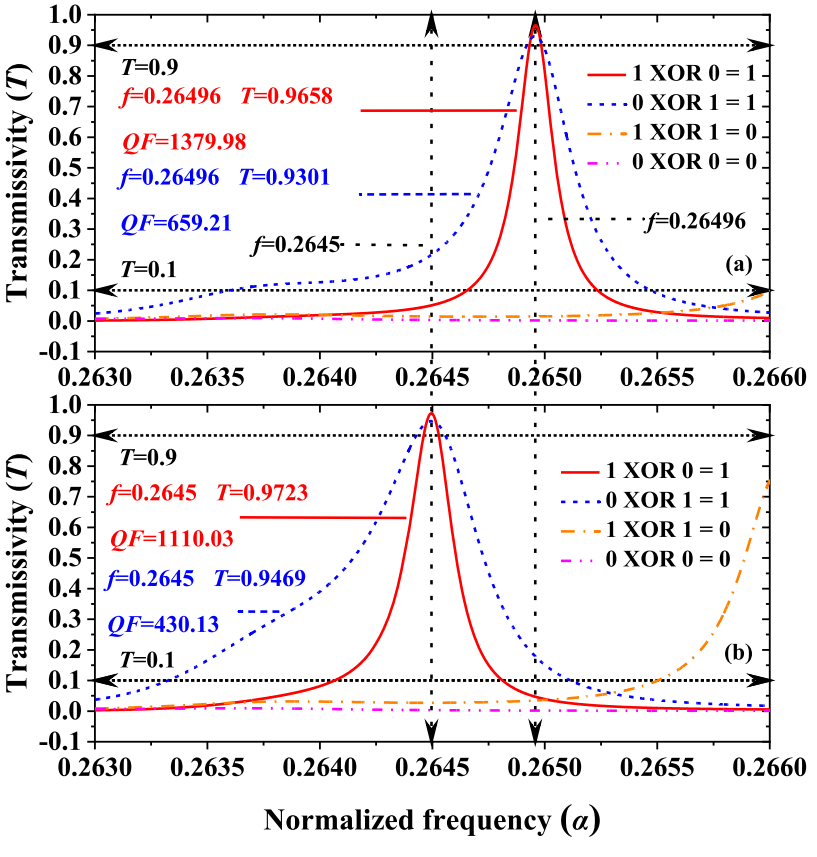

Figure 2. Schematic diagrams of magnetic controlled logic XOR operations and TP when EWs propagate. (a) The positive XOR logic operation and corresponding TP under magnetic field. (b) The negative XOR logic operation and corresponding TP under magnetic control.

Table 1. Truth value table belongs to the XOR logic gate (the parentheses indicate the presence state of the electric field and the value of T).

In_1	In_2	Ou_1
0	0	0 ($T < 0.1$)
1 (B_1 exists)	0	1 ($T > 0.9$)
0	1 (B_2 exists)	1 ($T > 0.9$)
1 (B_1 exists)	1 (B_2 exists)	0 ($T < 0.1$)

direction, as can be seen in Figure 2(b), the same logical relationship as when positive propagation, $T = 0.9723$, QF $= 1110.03$ at '1 XOR 0 $= 1$', $T = 0.9469$, QF $= 430.13$ match '0 XOR $1 = 1$', and the NAFP of TP in both cases is 0.2645 α, it is worth noting that the difference between the NAFP belonging to the positive and negative TP is 0.00046 α, which reflects the non-reciprocity of PCLT. Similarly, for '1 XOR $1 = 0$' and '0 XOR $0 = 0$', T is much less than 0.1. It can be seen that the transmission spectra of the PCLT designed in our work strictly adheres to the XOR logic gate function on both the negative and negative scales under the regulation of the external magnetic fields B_1 and B_2, and due to its non-reciprocity, the two scales can orchestrate logic operations of different NAFP to obtain different QF values. The logical truth table is shown in Table 1.

Since there are many cases in which TP is generated on the positive and negative scales the PCLT designed in this paper, to better explain the causes of TP, we choose the best situation in which B_2 exists and B_1 does not exist ($B_1 = 0$ T, $B_2 = 1.3$ T) to explain the phenomenon. Figure 3(a) shows the reflectivity (R) and T spectra in which B_1 is absent and B_2 is present at the negative scale when in-defect layer InSb is not introduced. It is clear from the figure that a wide PBG is formed between 0.244 α and 0.2653 α, and the T is close to 0 in this range, which means that EWs cannot propagate in this frequency band. When InSb is introduced into the PCLT as a defect layer, its corresponding transmission spectrum is shown in Figure 3(b). The original PBG finally formed a passband, which is caused by the introduction of the defect layer and the breaking of the symmetry of the original structure. In the designed structure, a sharp TP is generated, corresponding to a NAFP of 0.2645 α, $T = 0.9537$. To more clearly observe the propagation of TM polarization waves in PCLT, as shown in Figure 4, an electric field intensity distribution map with a normalized angular frequency ω of 0.2645 α is produced, and thus illustrates the formation principle of TP. In the case of $\omega = 0.2645\ \alpha$, the surface partial electric field of the defect layer $InSb_2$ is enhanced, which stimulates the localization defect mode resonance, resulting in a sharp TP. To highlight the importance of the defect layer, when B_2 exists and B_1 is absent on the negative scale, Figure 5(a) indicates that the transmission spectrum alters when the change occurs in the location of the defect layer. When the original defect layer $InSb_2$ moved behind the dielectric D layer, the T and QF of the TP decreased to 0.363 and 415.82, respectively, and there is no sharp TP ($T > 0.9$). At the same time, the resonant frequency of the TP changes from 0.2645 α to 0.264 α, indicating that the variation of the defect layer location affects the position of local electric field enhancement, thus affecting the resonant frequency. When the material of the defect layer is varied from $InSb_2$ to dielectric B, the change in TP reduction is shown in Figure 5(b). The corresponding T and QF are 0.6597 and 413.63, which is unable to reach the output logic level '1'. It can be seen that the location and material of

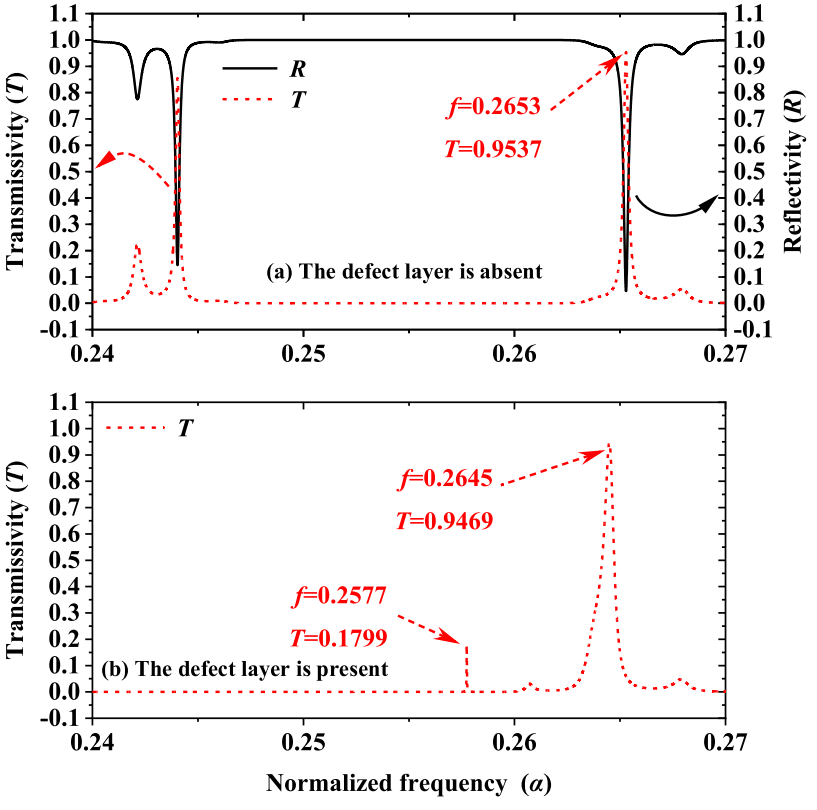

Figure 3. The simulation of effect of the defect layers on PBG under the condition of $B_1 = 0$ T and $B_2 = 1.3$ T when EWs propagate negatively: (a) R and T maps when no defects are introduced in the structure. (b) T spectrum after introducing defects.

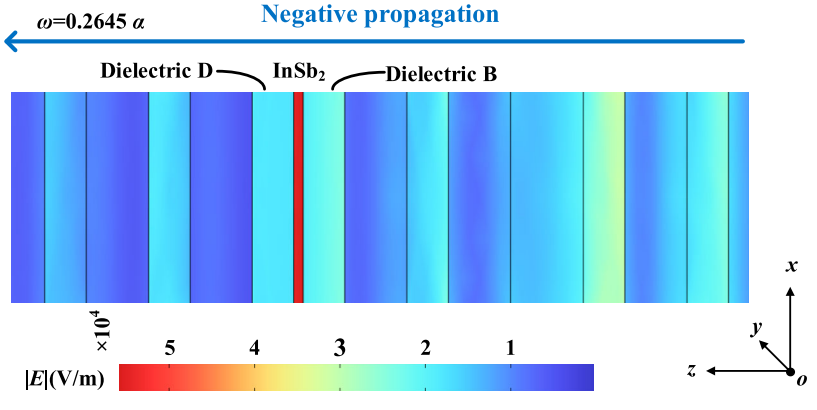

Figure 4. The electric field distribution diagram when EWs propagate negatively at $\omega = 0.2645\,\alpha$ under the condition of $B_1 = 0$ T and $B_2 = 1.3$ T on the negative scale.

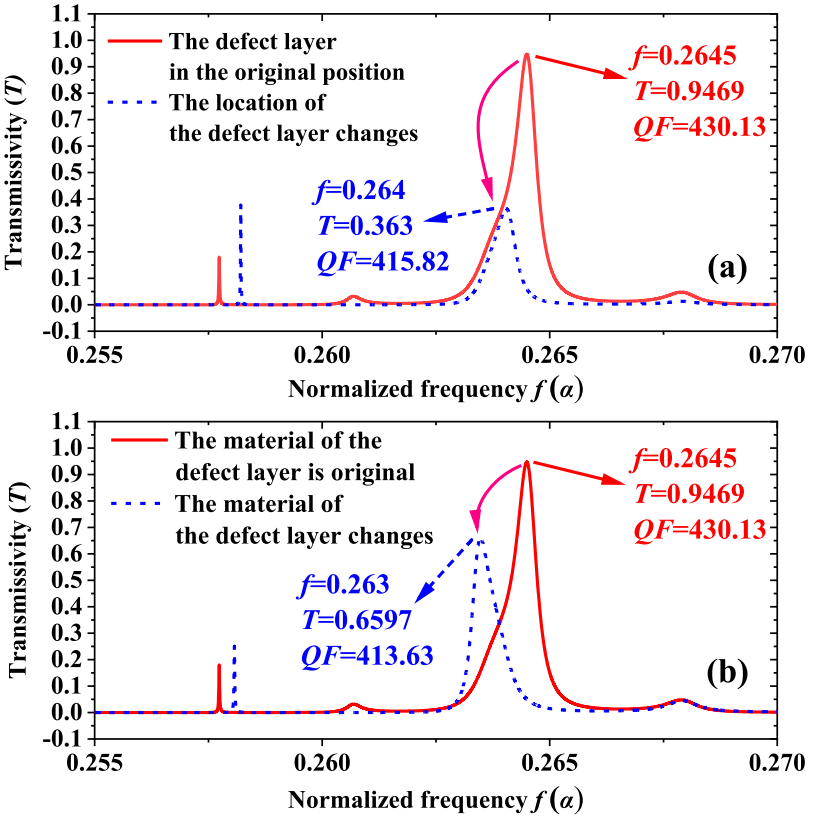

Figure 5. The transmission spectra on the negative scale when $B_1 = 0$ T and $B_2 = 1.3$ T. (a) The change occurs in the location of the defect layer. (b) The change occurs in the material of the defect layer.

the defect layer are crucial for the formation of sharp TP, and the correct selection will be conducive to better breaking PBG and forming a good passband.

In addition, the number of dielectric layer periods can also have a significant impact on TP, as shown in Figure 6. When $B_1 = 0$ T and $B_2 = 1.3$ T on the negative scale, only N_1 changes while keeping the number of other periods constant (in Figure 6(a)). When $N_1 = 6$, 7, or 8, the corresponding resonant frequency points are 0.2645 α, 0.2545 α, and 0.2644 α, along with the gradual reduction in T and QF, the shape of TP has little change. Under the condition that $N_2 = 4$, 5, or 6, the resonant peak moves to the place with a small frequency step by step, accompanied by the increase of T and the decrease of QF. When N_3 varies from 4 to 6, the peak shape changes greatly. Moreover, TP produces a redshift, and T increases gradually. The resonant peak frequency decreases with the increase of N_4, accompanied by the increase of T and QF. The results indicate that the change of period number has a great influence on the performance of resonant TP, mainly because the variation of a period number will alter the position and intensity of the local electric field, thus affecting the resonant frequency of TP and the values of T and QF.

To enhance the non-reciprocity of PCLT, in addition to introducing the magneto-optical medium InSb as a defect to break the symmetry of the original structure, our design also

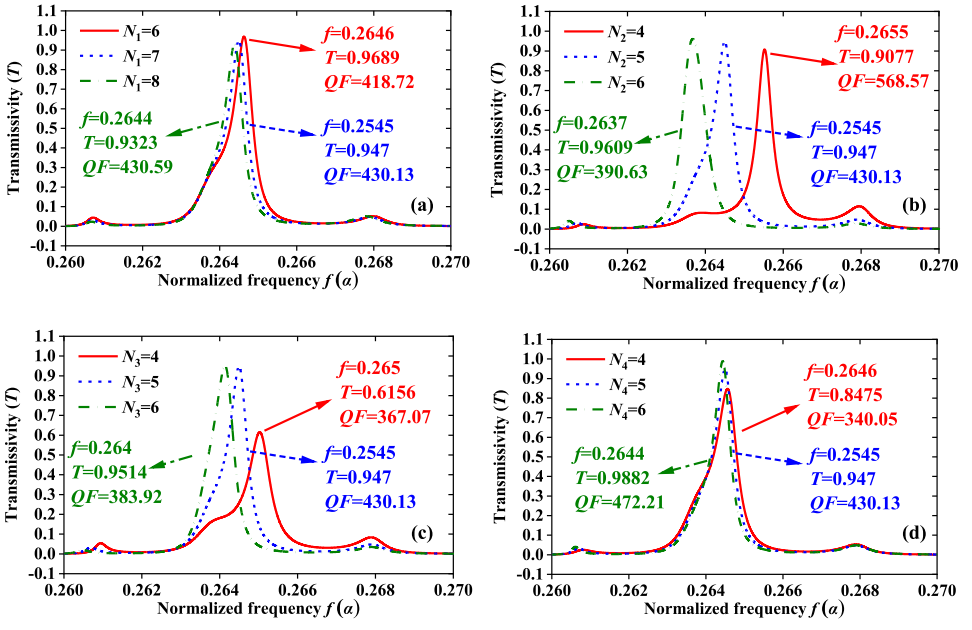

Figure 6. The effect of the number of periods on the TP under the condition of $B_1 = 0$ T and $B_2 = 1.3$ T on the negative scale. (a) $N_1 = 6$, 7 and 8. (b) $N_2 = 4$, 5 and 6. (c) $N_3 = 4$, 5 and 6. (d) $N_4 = 4$, 5 and 6.

increases the non-reciprocity of PCLT on the back and forth scales by increasing the incidence angle θ of EWs. Figure 7 discusses the non-reciprocal situation of TP at $B_1 = 0.85$ T and $B_2 = 0$ T when EWs propagate on the positive and negative scales, and it can be seen that the NAFP related to the positive TP represented by the red solid line and the negative TP indicated by the blue dotted line are almost coincident at the time of the vertical incidence of EWs ($\theta = 0°$), and the non-reciprocity is poor. However, as the angle continues to

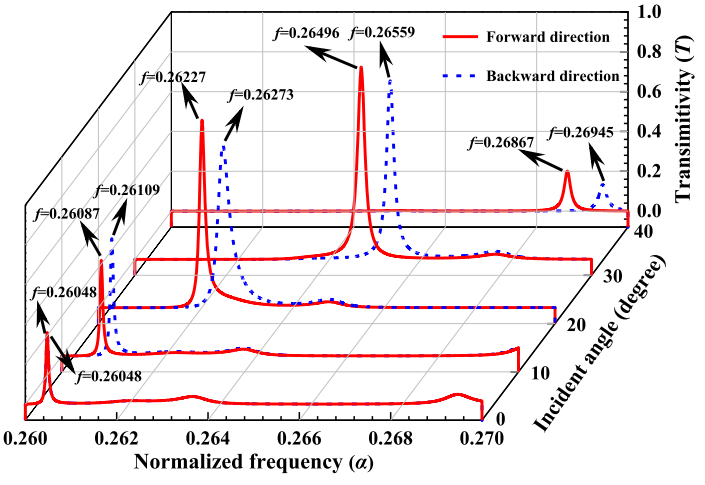

Incident angle (degree)	Frequency difference $\Delta f(\alpha)$
0	0
10	2.2×10^{-4}
20	4.6×10^{-4}
30	6.3×10^{-4}
40	7.8×10^{-4}

Figure 7. The effect of the incident angle on the non-reciprocal when B_1 exists and B_2 is absent on the positive and negative scales, $\theta = 0°$, 10°, 20°, 30° or 40°.

increase, the frequency gap as seen in the table between the positive and negative TP NAFP is also expanding, which symbolizes that the non-reciprocity of PCLT is increasing. Since the PCLT designed herein requires that the T of the positive and negative TP is as good as possible in non-reciprocity under the condition of satisfying higher than 0.9, that is, the angular frequency difference of the NAFPs belonging to and for scales is as large as possible, so we take $\theta = 30°$ as the anteroposterior incident angle of EWs.

When one of the external magnetic fields is fixed, the magnetized InSb PCLT can detect the other external magnetic field and still maintain good XOR logic operation function within the detection range, it is worth emphasizing that it can keep this function on positive and negative scales with disparate linear ranges and LFR, and the spatial distribution of T can be obtained by the transport matrix method. Figure 8 shows the x-y plane of the anteroposterior magnetic flux density B_1 detection and TP changing under different NAFPs, when B_1 varies and $B_2 = 0$ T, that is, the input LL is '$\text{In}_1 = 1$' and '$\text{In}_2 = 0$'. Moreover, as the magnetic flux B_1 intensity increases, non-reciprocal TP begins to show a continuous frequency shift and becomes more acute. As can be seen in Figure 8(a), for positive magnetic field detection, continuous TP exhibits a good LFR in the range of B_1 from 0.756 T to 0.99 T. In this range, the average of T is 0.9568, greater than 0.9. Figure 8(b) is a linear of 0.629 T to 0.838 T reflecting the negative propagation of EWs, and the average value of TP correlating to each NAFP is 0.9368, above 0.9, which satisfies the '$\text{Ou}_1 = 1$' of the output LL. When B_1 alters and B_2 is present, its anteroposterior x-y plane view is shown in Figure 9. It is obvious that no sharp TP exists and no linear range is formed that meets the requirements, which corresponds strictly to '1 XOR 1 $= 0$' in the XOR logic gate.

To better analyze the magnetic field detection performance of PCLT, when B_1 changes and B_2 does not exist, the LFR between the magnetic field strength B_1 and the related NAFP is taken sharp in Figure 10. It can be seen that the positive detection represented by the red solid line and the negative detection symbolized by the blue dotted line is well programed LFR. When B_1 is between 0.756 and 0.99 T, the LFR for positive detection is $f = 0.0072B_1 + 0.2588$, and 0.0072 α/T is its S. The R-square is 0.9994, which proves that the

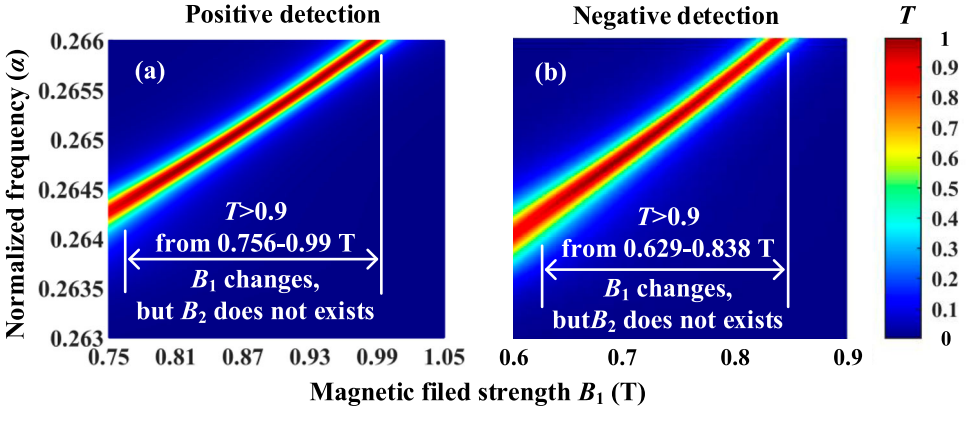

Figure 8. The top view of TP varies with the magnetic field B_1 and the NAFP, where B_1 exists and B_2 does not: (a) Changes in the TP of positive propagation, and the detection scope is 0.756–0.99 T. (b) Changes in the TP of negative propagation, and the detection scope is 0.629–0.838 T.

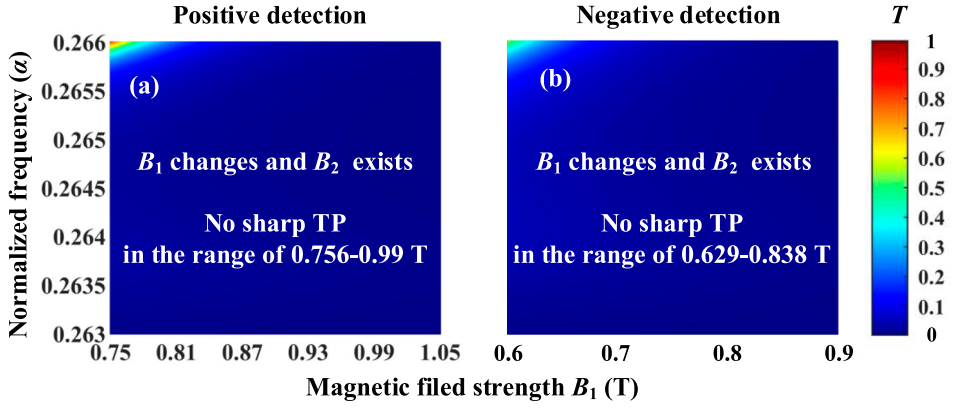

Figure 9. The top view of TP which varies with the magnetic field B_1 and the NAFP, where both B_1 and B_2 exist: (a) Changes in the TP of positive propagation, and no sharp TP in 0.756–0.99 T. (b) Changes in the TP of negative propagation, and no sharp in 0.756–0.99 T.

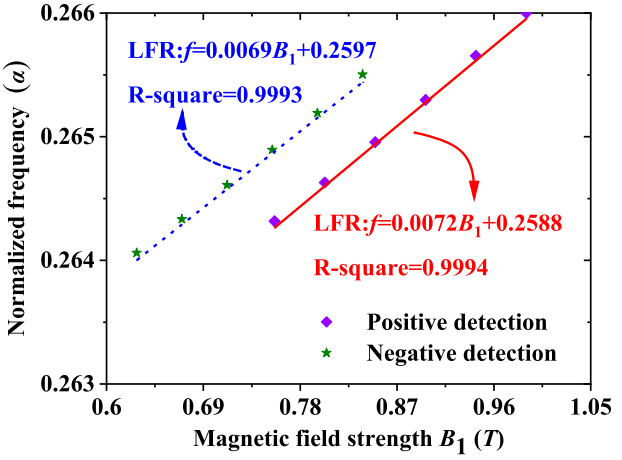

Figure 10. LFR between NAFP and magnetic field strength B_1 on the positive and negative sales when B_1 exists and B_2 does not.

linearity is very good and suitable for making sensors. Figure 11 shows the QF and FOM values for anteroposterior detection, which are evaluative of the sensor, and it can be seen that the QF and FOM values are generally rising as the B_1 intensity increases. Positive detection as shown in Figure 11(a), after calculation, its average QF, FOM, and DL are apart 1323.45, 35.93 T^{-1}, and 1.39 × 10^{-3} T, which means that the performance parameters of the sensor still have a certain competitive advantage. When the magnetic field is sensed negatively, its LFR is $f = 0.0069B_1 + 0.2597$ in the range of B_1 is 0.628 T to 0.838 T, R-square = 0.9993, and $S = 0.0069\ \alpha$/T, indicating that LFR is reliable. From Figure 11(b), it can be concluded that its QF, FOM, and DL averages are corresponding to 1163.52, 30.20 T^{-1}, and 1.65 × 10^{-3} T. As mentioned earlier, these sensing performance indicators can be made of multi-scale magnetic field B_1 sensing detector, and the measured range of the front and back directions is obviously different, which means that the measurement range of the entire structure is

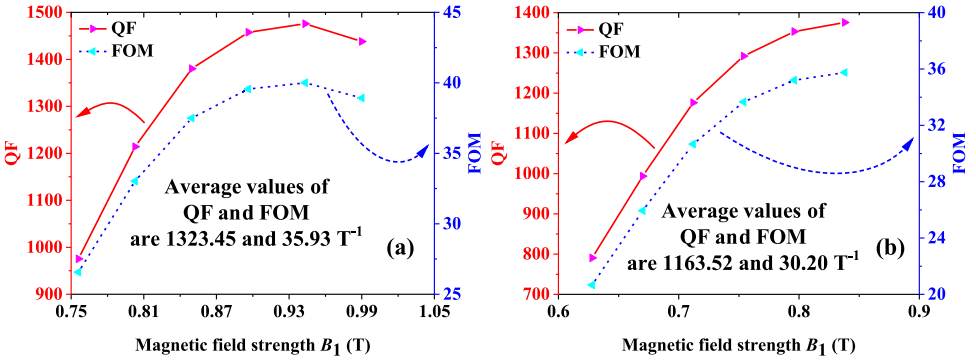

Figure 11. The QF and FOM at different B_1 under the condition of '1 XOR 0 = 1'. (a) The positive sensing, owning 1323.45 and 35.93 T^{-1} as the average values of QF and FOM. (b) The negative sensing, owning 1163.52 and 30.20 T^{-1} as the average values of QF and FOM.

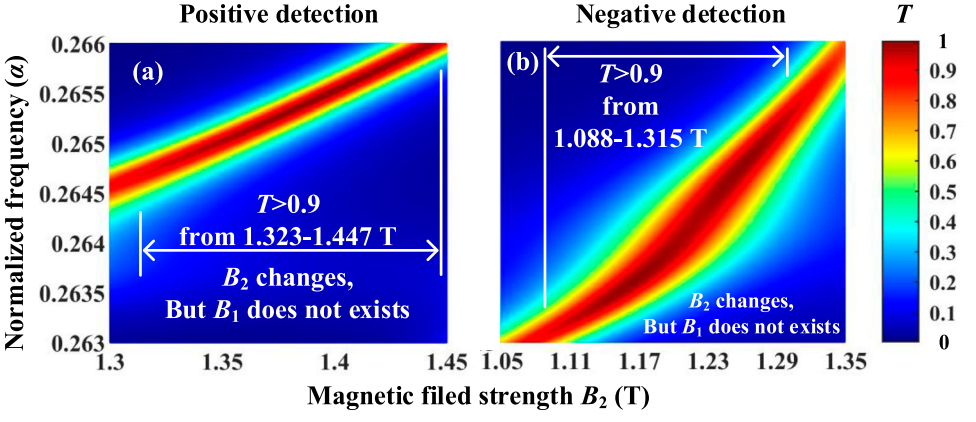

Figure 12. The top view of TP varies with the magnetic field B_2 and the NAFP, where B_2 exists and B_1 does not: (a) Changes in the TP of positive propagation, and the detection range is 1.323–1.447 T. (b) Changes in the TP of negative propagation, and the detection range is 1.088–1.315 T.

also expanded. Furthermore, in the same measurement range, different TP as to different QF, FOM, and DL can achieve magnetic field detection functions with different accuracy.

Under the condition that the external magnetic field $B_1 = 0$ T and B_2 is constantly changing, the PCLT proposed can still accurately detect the strength of B_2. First of all, the positive scale is analyzed in detail, Figure 12 is the *x*-*y* plane of the TP surface plot, which intuitively illustrates the relationship between the frequency of the normalized target resonant peak and B_2. The change in the strength of the magnetic field B_2 leads to the drift of TP, and when the EWs propagate positively, B_2 varies in the range of 1.323 T to 1.447, and 1.088 T to 1.315 T is the range of B_2 under the condition of negative EWs propagation. Their related T is greater than 0.9, the positive average is 0.9368 and the negative value is 0.9531, which meets the requirements of the position TP value. The positive LFR of B_2 emerges in Figure 13, the equation is $f = 0.01B_2 + 0.2515$, and the 0.01 α/T is its S, indicating that the magnetic flux detection is very sensitive. R-square = 0.9995 symbolizes that it exhibits excellent linearity over the detection range. As appeared in Figure 14(a), 689.32 and

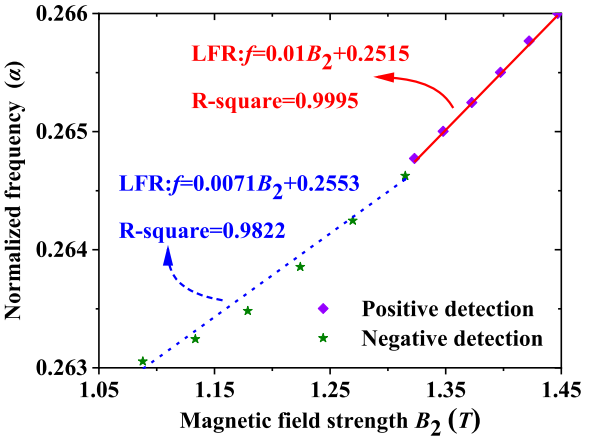

Figure 13. LFR between NAFP and magnetic field strength B_2 on the positive and negative sales when B_1 exists and B_1 does not.

25.96 T^{-1} severally correlate to the averages of QF and FOM. In Figure 13, when detected negatively, the LFR is $f = 0.0071B_2 + 0.2553$, $S = 0.0071\ \alpha$/T, and R-square $= 0.9822$, showing an acceptable linearity. It can be seen from Figure 12(b) that the TP in the front and rear segments of the detection range is very sharp. However, the sharpness decreases significantly in the middle part, corresponding to Figure 14(b), the QF and FOM values of TP have dropped significantly in the middle part, and the average values of QF and FOM are 492.01 and 13.25 T^{-1}. For positive and negative detection, the average DL is about 1.02×10^{-3} T and 3.78×10^{-3} T, enabling more accurate magnetic flux density detection. When the applied external magnetic field B_2 is constantly changing, and the value of B_1 is present and fixed, for the forward scale, $B_1 = 0.85$ T, $B_1 = 0.695$ T on the negative scale, and the x-y floor plan is displayed as occurred in Figure 15. It can be seen that there is no TP and LFR, matching the '1 XOR 1 = 0' of the XOR logical operation. In summary, the PCLT can perform accurate and wide-ranging magnetic field detection and can meet the XOR logic operation function.

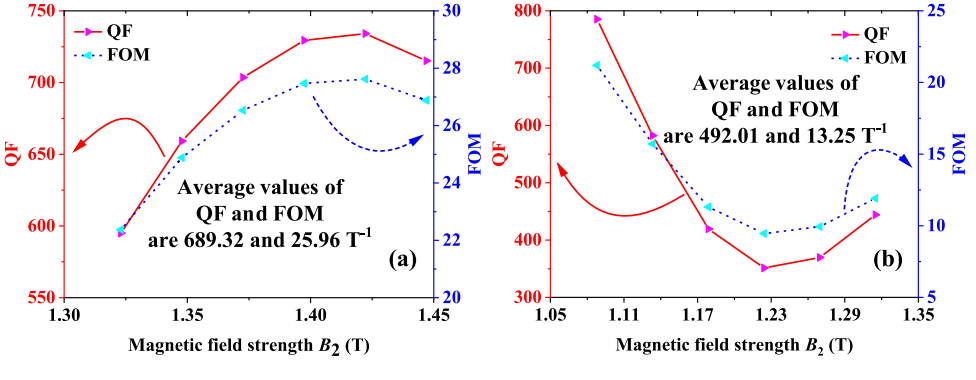

Figure 14. The QF and FOM at different B_1 under the condition of '0 XOR 1 = 1'. (a) The positive sensing, owning 689.32 and 25.96 T^{-1} as the average values of QF and FOM. (b) The negative sensing, owning 492.01 and 13.25 T^{-1} as the average values of QF and FOM.

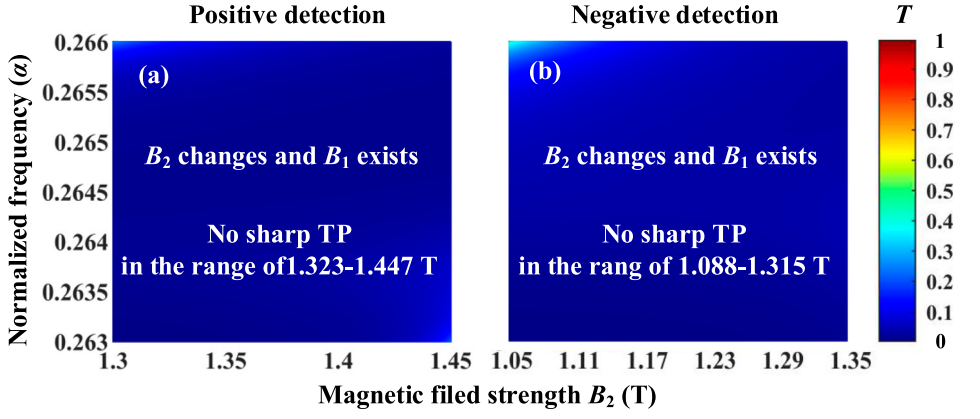

Figure 15. The top view of TP varies with the magnetic field B_2 and the NAFP, where both B_1 and B_2 exist: (a) Changes in the TP of positive propagation, and no sharp TP in 1.323–1.447 T. (b) Changes in the TP of negative propagation, and no sharp TP in 1.088–1.315 T.

In the field of biology, chemistry, physics and so on, there is an urgent need for the identification of the RI of substances, so the sensors designed for RI detection are very extensive. The PCLT sensor designed not only can realize magnetic field sensing detection, but also can sense and detect RI. To study the ability of PCLT to detect RI and the XOR logic operation function, when RI alters within a certain range, we set the medium n_C to the sensitive part, and the RI sensing function of PCLT is suitable for RI measurement of n_C. Figure 16 indicates an *x*-*y* plan diagrams of the four logical cases in which XOR logic operates when EWs propagate positively. As shown in Figure 16(a) and (b), when one of B_1 and B_2 exists and the other is not present, both the TP and its corresponding NAFP form a good LFR within their RI detection range, and their T average values coinciding to 0.9634 and 0.9715 in several, which is much greater than 0.9, ensuring that the output LL is '$Ou_1 = 1$'. When both B_1 and B_2 are existent or both are absent, as assumed in Figure 16(c) and (d), no sharp TP appears. This means that the RI detection on the positive scale is strictly followed the XOR logical operations '1 XOR 0 = 1', '0 XOR 1 = 1', '1 XOR 1 = 0' and '0 XOR 0 = 0'. It can be objectively seen from Figure 17 that when the EWs are propagated forward, the detection range of the RI of n_C is 1.3–1.65 under the condition of maintaining $B_1 = 0.85$ T, $B_2 = 0$ T, and the corresponding LFR is $f = -0.0009n_C + 0.2662$, -0.0009 α/RIU is S, and the R-square of the equation is 0.9999, explaining excellent linearity. When $B_1 = 0$ T and $B_2 = 1.343$ T, the LFR correlating to n_C in the detection range of 1.33–1.65 is $f = -0.0038n_C + 0.2707$, $S = -0.0038$ α/RIU, and R-square = 0.9935, which has good linearity. The QF and FOM values related to the above two cases are demonstrated in Figure 18, when input LL '$In_1 = 1$' and '$In_2 = 0$', after calculation, the average values of their corresponding QF, FOM, and DL are shown in Figure 18(a), which are 1381.88, 4.7 RIU^{-1} and 0.011 RIU, separately. Figure 18(b) shows a dotted line plot of QF and FOM values at '$In_1 = 0$' and '$In_2 = 1$', which shows that as n_C increases, both QF and FOM take on a rapid downward trend, belonging to the gradual decrease in sharpness of TP in Figure 16(b). However, its QF, FOM and DL averages are 541.64, 7.78 RIU^{-1}, and 6.42×10^{-3} RIU, respectively, which can meet the sensing performance requirements. The results show that the designed PCLT has good RI detection performance in the case of '1 XOR 0 = 1' and '0 XOR 1 = 1' on the

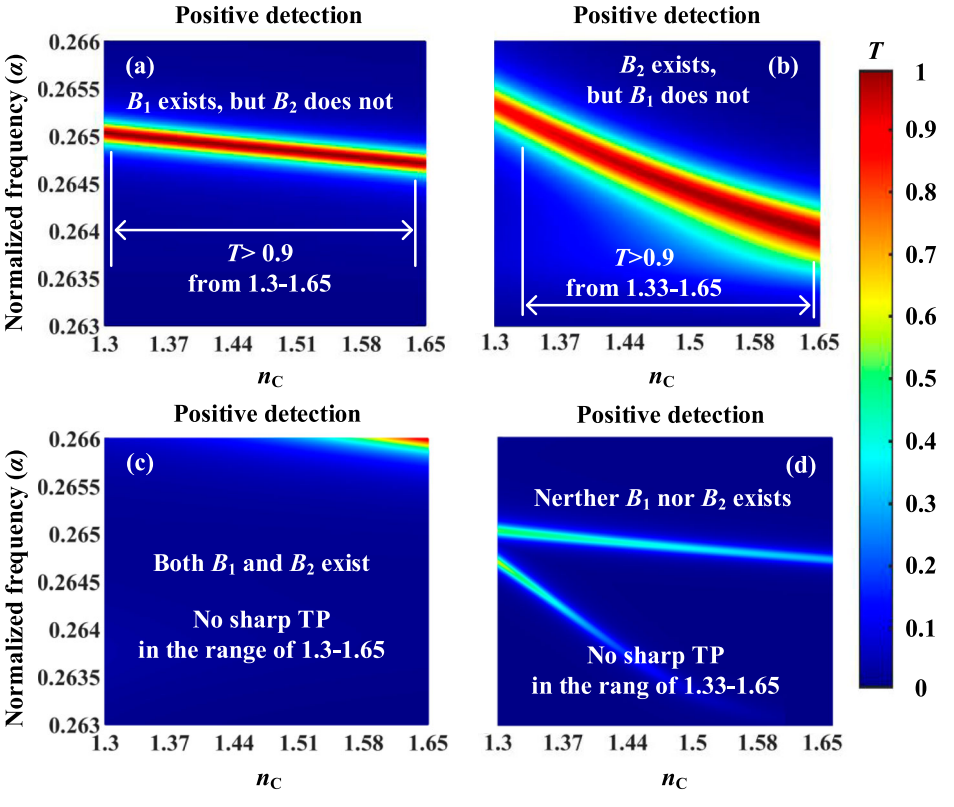

Figure 16. The top view of TP varies with the RI of n_C and the NAFP when EWs propagate positively. (a) Changes in the TP when B_1 exists but B_2 does not, and the detection range is 1.3–1.65. (b) changes in the TP when B_2 exists but B_1 does not, and the detection is 1.33–1.65. (c) changes in the TP when both B_1 and B_2 exist, and no sharp TP in 1.3–1.65. (d) changes in the TP when neither B_1 nor B_2 exists, and no sharp TP in 1.33–1.65.

positive scale. In addition, compared with the case of '$\mathrm{In}_1 = 1$' and '$\mathrm{In}_2 = 0$', the situation of '$\mathrm{In}_1 = 0$' and '$\mathrm{In}_2 = 1$' has a smaller DL and a larger FOM, which means that it exists greater sensitivity in the same detection range.

For RI sensors, due to the presence of B_1 on the forward scale, when B_2 is absent, the RI detection range of n_C is 1.3–1.65. In a similar way, when B_1 is not present but B_2 is subsistent, the RI of n_C owns a detection range of 1.33–1.65. So the range of 1.33–1.65 is the common detection range belonging to these two cases. Therefore, we set the dielectric later n_C as a sensitive region and use it to achieve the purpose of biological sensing, which can detect substances when RI alters in the range of 1.33–1.65, such as the sensing detection of the concentration of glucose aqueous solution (C_G). The RI change of glucose aqueous solution is close to the variation in blood glucose concentrations, and the study of the former can provide a certain basis for the research and development of the latter. The aqueous solution of glucose is fed into the sensing region, and the C_G and the corresponding n_G form LFR, which can be expressed as [30]:

$$n_G = 1.33230545 + 0.00011889C_G. \tag{13}$$

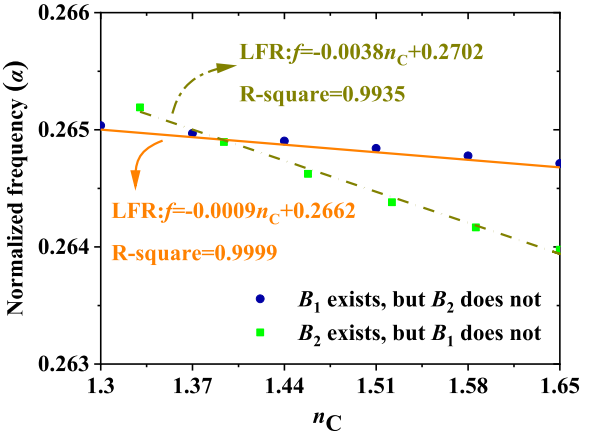

Figure 17. LFR between NAFP and RI of n_C on the positive sale when '1 XOR 0 = 1' and '0 XOR 1 = 1'.

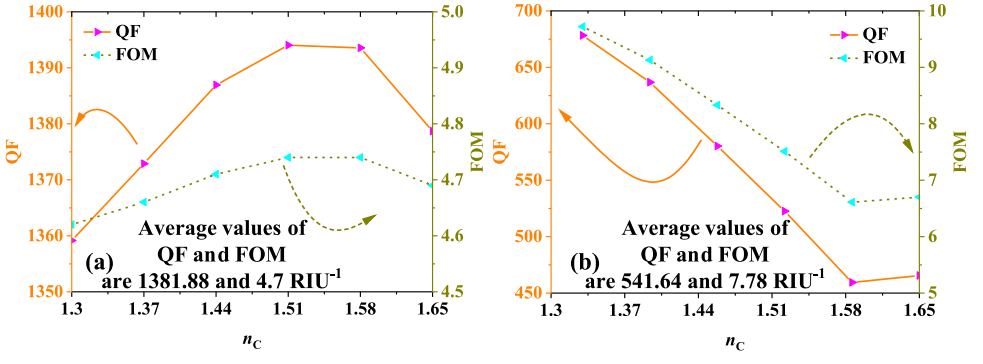

Figure 18. The QF and FOM at different n_C under the condition of positive propagation. (a) In the case of '1 XOR 0 = 1', owing 1381.88 and 4.7 RIU^{-1} as the average values of QF and FOM. (b) In the case of '0 XOR 1 = 1', owing 541.64 and 7.78 RIU^{-1} as the average values of QF and FOM.

When the CG is in the range of 140–330 g/L, the corresponding RI range is 1.3489–1.3715, and accurate RI detection can be achieved within the detection range 1.33–1.65 on the positive scale. As can be seen from Figure 17, it can show good LFR at both '1 XOR 0 = 1' and '0 XOR 1 = 1', which is expected to provide a new pathway for microscopic observation of blood glucose concentrations in medicine.

For EWs negative propagation, Figure 19 depicts an *x*-*y* plan for all the logical operation cases. For the two cases of '1 XOR 0 = 1' and '0 XOR 1 = 1', Figure 19(a) and (b) respectively represent the RI of their n_C and the LFRs of NAFP, and their TP means are 0.9669 and 0.9786, which are greater than 0.9, meeting the output LL requirement of '$Ou_1 = 1$'. As can be seen from Figure 19(c) and (d), there is no sharp TP generated, corresponding to the XOR logical operation function of '1 XOR 1 = 0' and '0 XOR 0 = 0'. As shown in Figure 20, the LFR of RI and NAFP is plotted, and when $B_1 = 0.695$ T, $B_2 = 0$ T, in the range of RI is 1–1.3, its LFR is $f = -0.0012n_C + 0.2661$, *R*-square = 0.9928. When $B_1 = 0$ T and $B_2 = 1.3$ T, $f = -0.0061n_C + 0.2728$ is its LFR at RI = 1.12–1.3, *S* is −0.0012 α/RIU, and 0.9998 is its *R*-square marking good linearity. Figure 21 is the related QF and FOM value plot of the two

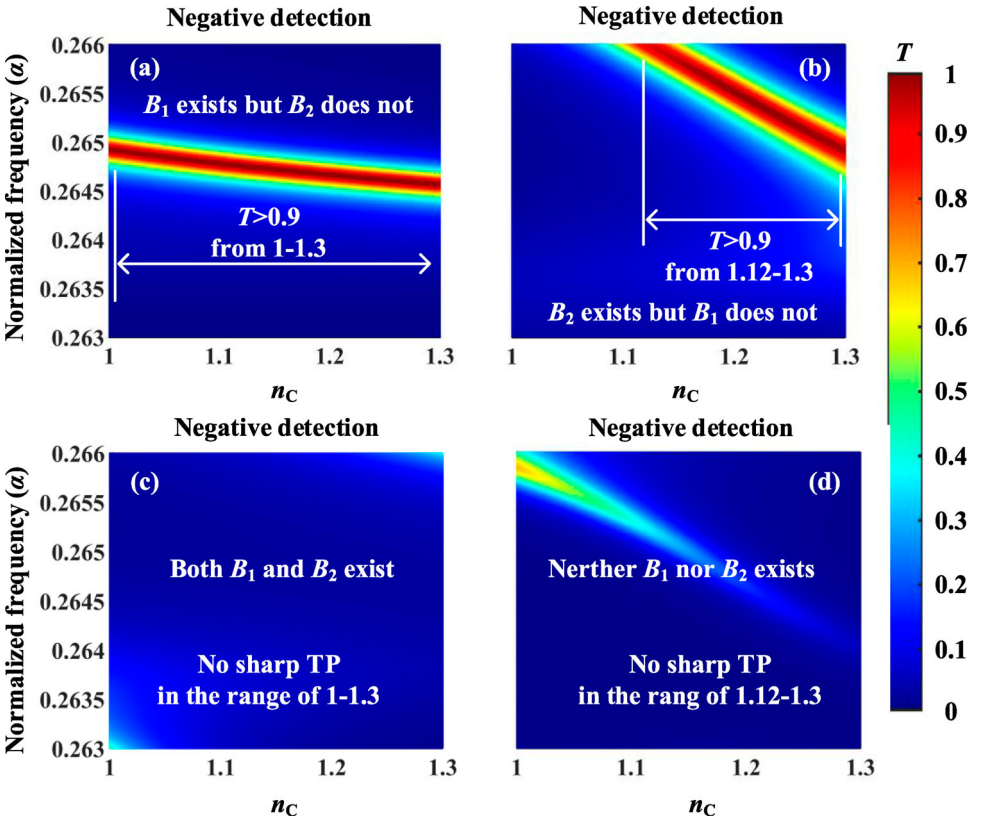

Figure 19. The top view of TP varies with the RI of n_C and the NAFP, when EWs propagate negatively. (a) Changes in the TP when B_1 exists but B_2 does not, and the detection range is 1–1.3. (b) changes in the TP when B_2 exists but B_1 does not, and the detection range is 1.12–1.3. (c) changes in the TP when both B_1 and B_2 exist, and no sharp TP in 1–1.3. (d) changes in the TP when neither B_1 nor B_2 exists, and no sharp TP in 1.12–1.3.

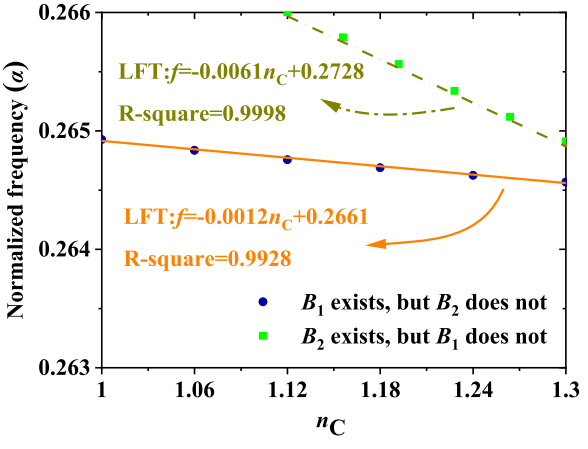

Figure 20. LFR between NAFP and RI of n_C on the negative sale when '1 XOR 0 = 1' and '0 XOR 1 = 1'.

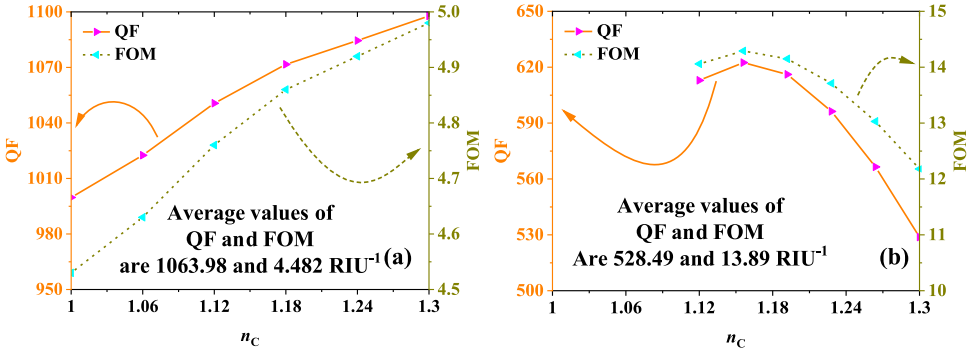

Figure 21. The QF and FOM at different n_C under the condition of negative propagation. (a) In the case of '1 XOR 0 = 1', owning 1063.98 and 4.482 RIU^{-1} as the average values of QF and FOM. (b) In the case of '0 XOR 1 = 1', owning 528.49 and 13.89 RIU^{-1} as the average values of QF and FOM.

cases, from the figure can be seen that at $n_C = 1.3$, QF in the case of '$In_1 = 1$', '$In_2 = 0$' to reach the maximum value of 1097.79, T reaches 0.9728. When '$In_1 = 0$', and '$In_2 = 1$', the QF reaches the minimum value of 528.76, and T is 0.9748, indicating that the sensor still has ideal selectivity. The corresponding average QF, FOM, and DL values are 1063.98, 4.482 RIU^{-1}, 0.01 RIU, and 528.49, 13.89 RIU^{-1}, 3.73×10^{-3} RIU in several, meeting the performance parameters of the production sensor. This article takes 1.12–1.3 as the common range of RI detected at the negative scale using '1 XOR 0 = 1' and '0 XOR 1 = 1'. Since the RI of the material measured by PCLT in our design does not depend on the frequency change of non-dispersion, the inclusion of different substances under test into the n_C in the sensitive region will produce different resonance frequencies, so the RI of this substance can be calculated by using the respective linear fitting equations of the above two logical cases to achieve the purpose of identifying the material. For example, when B_1 is present and B_2 is not, the unknown gas is passed into the n_C, and the NAFP is measured to be 0.26466 α, according to the LFR $f = -0.0012n_C + 0.2661$, the calculation can be seen that its RI is 1.2, correlating to carbon dioxide. For the absence of B_1, the presence of B_2 is also accurately detected on the basis of this principle of RI. It can be seen that by using the non-reciprocity of PCLT, the detection of different RI ranges on the positive and negative scales can be realized, which greatly improves the range and front-back functional selectivity of PCLT RI sensing detection.

From the above research discussion, it can be concluded that the designed PCLT in our work has performance values that can meet the requirements of magnetic field sensing and RI sensing on the anteroposterior scales. Due to the good non-reciprocity of PCLT, the corresponding NAFP for magnetic flux and RI detection varies greatly in the measurement range as EWs propagate in the opposite direction. The S, QF, and FOM of PCLT on the positive and negative scales are quite different, have excellent anteroposterior detection selectivity, and can achieve magnetic field and RI detection with different accuracy due to different DL. As shown in Table 2, the physical quantity sensing function of the PCLT designed in this work is based on the premise of XOR logic operation function, from the input LL 'In_1', 'In_2' and the corresponding output LL 'Ou_1', it can be seen that it strictly follows the XOR logic operation function of '1 XOR 0 = 1', '0 XOR 1 = 1', '1 XOR 1 = 0' and '0 XOR 0 = 0'. In addition,

Table 2. The performance parameters of the proposed PCLT sensors compare with the published sensors.

Reference		Scope of magnetic field	Scope of RI	Logic
Ref.[31]		0.14 T ~ 0.22 T	none	None
Ref.[30]		None	1.3323 ~ 1.35612	None
Ref.[32]		None	None	OR and XOR logic
This work	positive	0.756 T ~ 0.99 T	1.3 ~ 1.65	XOR logic
		1.323 T ~ 1.447 T	1.33 ~ 1.65	
	negative	0.628 T ~ 0.99 T	1 ~ 1.3	
		1.088 T ~ 1.315 T	1.12 ~ 1.3	

it also has a broader detection range and a variety of physical quantity detection functions at multiple scales.

4. Conclusion

Our work proposes a 1-D PCLT that can integrate a logical operation function and a plurality of physical quantity sensing detection functions, and it also takes advantage of non-reciprocity on the positive and negative scales. PCLT utilizes sharp TP ($T > 0.9$) produced by localization defect mode resonances and utilizes magnetic field regulation to implement XOR logic operations with high QF values. Changing the magnetic field strength and RI size, through the locking of the mobile TP NAFP, due to its high *S*, *R*-square, FOM, and low DL, the precise physical quantity sensing function can be realized. For magnetic field and RI sensing, on the positive scale, their corresponding sensing ranges are 0.756 T–0.99 T, 1.323 T–1.447 T, and 1.33–1.65, respectively. On the negative scale, the related sensing ranges are 0.628 T–0.99 T, 1.088 T–1.315 T, and 1.12–1.3 in several. In summary, the proposed 1-D PCLT has multiscale and multifunction, which is complementary to a single function and single scale and has a strong theoretical research prospect.

Disclosure statement

No potential conflict of interest was reported by the author(s).

Funding

This work was supported by the National College Student Innovation Training Program (grant number202210293014Z).

References

[1] Awad MA, Aly AH. Experimental and theoretical studies of hybrid multifunctional TiO_2/TiN/TiO_2. Ceram Int. 2019;45(15):19036–19043.
[2] Guo B. Photonic band gap structures of obliquely incident electromagnetic wave propagation in a one-dimension absorptive plasma photonic crystal. Phys Plasmas. 2009;16(4):043508.
[3] Qi L, Yang Z, Lan F, et al. Properties of obliquely incident electromagnetic wave in one-dimensional magnetized plasma photonic crystals. Phys Plasmas. 2010;17(4):042501.
[4] Guo B, Xie MQ, Peng L. Photonic band structures of one-dimensional photonic crystals doped with plasma. Phys Plasmas. 2012;19(7):072111.

[5] Aly AH, Mohamed D, Mohaseb MA. Theoretical and simulation study in defective semiconductor layer that incorporated with superconducting-dielectric photonic crystal. Int J Mod Phys B. 2019;33(32):1950397.
[6] Aly AH, Sayed FA. THz cutoff frequency and multifunction $Ti_2Ba_2Ca_2Cu_3O_{10}$/GaAs photonic bandgap materials. Int J Mod Phys B. 2020;34(10):2050091.
[7] Chiasera A, Scotognella F, Criante L, et al. Disorder in photonic structures induced by random layer thickness. Sci Adv Mater. 2015;7(6):1207–1212.
[8] Shaban M, Ahmed AM, Abdel-Rahman E, et al. Tunability and sensing properties of plasmonic/1D photonic crystal. Sci Rep. 2017;7(1):1–10.
[9] El Abouti O, El Boudouti EH, El Hassouani Y, et al. Optical tamm states in one-dimensional superconducting photonic crystal. Phys Plasmas. 2016;23(8):082115.
[10] Soltani O, Francoeur S, Baraket Z, et al. Tunable polychromatic filters based on semiconductor-superconductor-dielectric periodic and quasi-periodic hybrid photonic crystal. Opt Mater (Amst). 2021;111(15):110690.
[11] Park H, Camper A, Kafka K, et al. High-order harmonic generations in intense MIR fields by cascade three-wave mixing in a fractal-poled LiNbO_3 photonic crystal. Opt Lett. 2017;42(19):4020–4023.
[12] Olyaee S, Dehghani AA. High resolution and wide dynamic range pressure sensor based on two-dimensional photonic crystal. Photonic Sensors. 2012;2(1):92–96.
[13] Yang YP, Lin KC, Yang IC, et al. All-optical photonic crystal AND gate with multiple operating wavelengths. Opt Commun. 2013;297:165–168.
[14] Rao S-S, Zhang J-T, Zhang H-F. A multifunctional and multiscale device of magnetic-controlled AND logical operation and detection based on the nonreciprocity of the magnetized InSb photonic structure. Results Phys. 2021;31:105058.
[15] Hu B, Wang QJ, Zhang Y. Slowing down terahertz waves with tunable group velocities in a broad frequency range by surface magneto plasmons. Opt Express. 2012;20(9):10071–10076.
[16] Ardakani AG. Tunability of absorption with temperature in the terahertz regime based on photonic crystals containing graphene and defect InSb layers. Eur Phys J B. 2015;88(7):1–8.
[17] Fan F, Chang SJ, Gu WH, et al. Magnetically tunable terahertz isolator based on structured semiconductor magneto plasmonics. IEEE Photonics Technol Lett. 2012;24(22):2080–2083.
[18] Wan B, Zhang H, Wang P. Nonreciprocal absorber with a narrow band of angular polarization sensitive regions based on a quasi-periodic structure. Opt Lett. 2021;46(8):1934–1937.
[19] Xu ZL. Nonreciprocal properties of one-dimensional magnetized plasma photonic crystals. Hejubian Yu Dengliziti Wuli/Nucl Fusion Plasma Phys. 2018;38(1):117–124.
[20] Fatima S, Rani P, Kalra Y, et al. Design of AND logic gate using NAND gate in photonic crystal waveguides. Photonic fiber and crystal devices: advances in materials and innovations in device applications X. 9958, 2016, p. 153–159.
[21] Sharma S, Kumar J. Numerical analysis of optical logic gate based on nonlinear optical loop mirror with a photonic crystal fiber. J Nonlinear Opt Phys Mater. 2015;24(2):1550019.
[22] Yan X, Wang Y, Cheng T, et al. Photonic crystal fiber SPR liquid sensor based on elliptical detective channel. Micromachines (Basel). 2021;12(4):408.
[23] Guo S, Hu C, Zhang H. Ultra-wide unidirectional infrared absorber based on 1D gyromagnetic photonic crystals concatenated with general Fibonacci quasi-periodic structure in transverse magnetization. J Opt. 2020;22(10):105101.
[24] Xuan L, Kong X, Wu J. A smoothly-connected crescent transverse gradient coil design for 50mT MRI system. Appl Magn Reson. 2021;52(6):649–660.
[25] Nayak C, Bezerra CG, Costa CH. Photonic transmission spectra in graphene-based Gaussian random multilayers. Opt Mater (Amst). 2020;104:109838.
[26] Wan BF, Xu Y, Zhou ZW, et al. Theoretical investigation of a sensor based on one-dimensional photonic crystals to measure four physical quantities. IEEE Sens J. 2021;21(3):2846–2853.
[27] Chen S, Fan F, Wang X, et al. Terahertz isolator based on nonreciprocal magneto-metasurface. Opt Express. 2015;23(2):1015–1024.
[28] Trokhimchuck PP. Some electro-physical properties of InSb and InAs layers that were received with the help of methods of relaxed optics. Second International Conference on Advanced Optoelectronics and Lasers. 7009; 2008, p. 49–56.

[29] Ghasempour Ardakani A, Kalantari T, Nadgaran H. Tunable terahertz bistability with temperature in photonic crystals containing an InSb layer and coupled nonlinear defects. Eur Phys J B. 2015;88(9):1–5.
[30] Ghorbani S, Sadeghi M, Adelpour Z. A highly sensitive and compact plasmonic ring nanobiosensor for monitoring glucose concentration. Laser Phys. 2020;30(2):026204.
[31] Atalay S, Kaya AO, Kolat VS, et al. One-dimensional magnonic crystal for magnetic field sensing. J Supercond Novel Magn. 2015;28(7):2071–2075.
[32] Kabilan AP, Susan Christina X, Elizabeth Caroline P. Photonic crystal based all optical OR and XO logic gates. In: 2010 Second International conference on Computing, Communication and Networking Technologies IEEE, 2010.